Thermally-activated post-growth dewetting of fullerene C$_{60}$ on mica

Sebastian Bommel[1,2]**, Holger Spranger**[2]**, C. Weber**[2]**, N. Kleppmann**[3]**, Stephan V. Roth**[1]**, S. H. L. Klapp**[3]**, and Stefan Kowarik***[,2]

[1] Deutsches Elektronen-Synchrotron (DESY), Notkestr. 85, 22607 Hamburg, Germany
[2] Institut für Physik, Humboldt-Universität Berlin, 12489 Berlin, Germany
[3] Institut für Theoretische Physik, Technische Universität Berlin, 10623 Berlin, Germany

* Corresponding author: e-mail stefan.kowarik@physik.hu-berlin.de

Understanding and controlling the growth and stability of molecular thin films on solid surfaces is necessary to develop nanomaterials with well-defined physical properties. As a prominent model system in organic electronics, we investigate the post-growth dewetting kinetics of the fullerene C$_{60}$ on mica with real-time and *in situ* X-ray scattering. After layer-by-layer growth of C$_{60}$, we find a thermally-activated post-growth dewetting, where the smooth C$_{60}$-layer breaks up into islands. This clearly shows that growth is kinetically limited before the system moves over an activation barrier into an energetically favored configuration. From the temperature-dependent dewetting kinetics we find an effective activation barrier of 0.33 eV, which describes both the temperature-dependent macroscopic changes in the surface morphology and the microscopic processes of inter- and intralayer diffusion during dewetting.
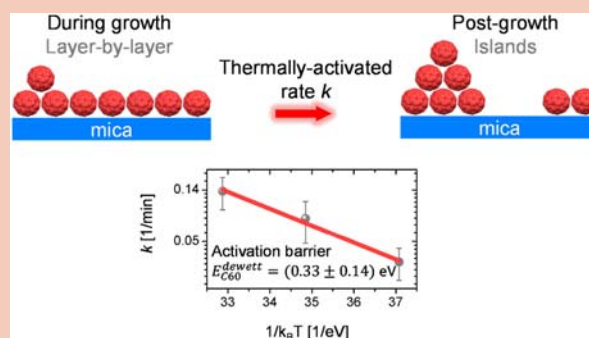
1 Introduction The thin film morphology is a key parameter for an optimized design of organic heterostructures and organic devices with high performance [1–3]. The morphology formation of organic thin films can be controlled by templating or epitaxial relations with the substrate [4, 5] as well as the choice of growth conditions [6–12], but post-growth dynamics, such as the break-up of a smooth thin film into islands, are crucial both for further processing steps as well as for the long-term device stability [13]. Post-growth reorganization is particularly common for molecular soft matter films and has been observed for several technologically relevant molecular materials [14] including diindenoperylene [15], pentacene [16] and fullerene C$_{60}$ [17, 18]. For C$_{60}$ on alkali halides, a spontaneous post-growth dewetting phenomenon has been pro-

posed, where an island formation is favored after the growth [17].

However, the understanding of post-growth dewetting kinetics is lacking, and in particular a quantification of the corresponding energetics is largely missing. Unravelling the rate constants of the post-growth processes and revealing the impact of temperature is essential for rational device design and yields a broader fundamental understanding of molecular reorganization processes in general. The previously found C$_{60}$ dewetting [17] due to weak molecule-substrate interaction for C$_{60}$ on insulating surfaces such as alkali halides or the muscovite mica [19] makes fullerene C$_{60}$ on mica an appropriate model system to study the kinetics of post-growth dynamics.

Phys. Status Solidi RRL **9**, No. 11 (2015)

647

Here, we use real-time and *in situ* X-ray scattering to shed light on the post-growth dewetting kinetics of fullerene C_{60} on crystalline muscovite mica [20]. We find a thermally-activated post-growth dewetting. A temperature increase of 40 K results in a five-time larger upward mass transport during dewetting. From our temperature-dependent measurements an effective activation barrier of 0.33 eV for the C_{60} dewetting is quantified for the first time. It describes the temperature dependence and timescale of changes in the surface morphology from a layer to a dewetted island configuration as well as microscopic diffusion- and step-edge crossing processes.

2 Experiment For information on the evolution of the vertical morphology during film formation and during post-growth dewetting, we monitored the X-ray reflectivity (XRR) at the so called anti-Bragg position which corresponds to half the q-value of the C_{60} (111) Bragg-reflection. Thin films of fullerene C_{60} (Sigma-Aldrich, >99.5% purity) were grown under high vacuum conditions with a base pressure of 10^{-7} mbar on freshly cleaved mica (Plano GmbH) for substrate temperatures of 40 °C, 60 °C or 80 °C to reveal the influence of temperature on the post-growth dewetting process. The deposition rate of 1 Å/min was controlled by a quartz crystal micro balance. Films were fabricated repeatedly on the same substrate, intermittently heating the mica substrate to ~450 °C for more than one hour to clean by re-evaporating previously grown molecules. Cleanliness of the surfaces after re-evaporation was checked using XRR. No changes were observed and C_{60} film growth was reproducible. Mica-C_{60} epitaxy as known from Ref. [4] was confirmed with grazing incidence X-ray diffraction (GIXD). The *in situ* X-ray scattering measurements of growth and post-growth dewetting, as well as GIXD were performed on a lab based diffractometer with a Cu K_{α} rotating anode source. Real-time XRR measurements of the multilayer film formation for a temperature of 60 °C were carried out at the beamline P03 at PETRA III/ DESY [21] at a wavelength of 0.946 Å. The atomic force microscopy (AFM) images presented here were recorded with a JPK NanoWizard® II in tapping mode.

3 Results X-ray scattering is a versatile tool to investigate the vertical morphology formation of organic thin films in real time and non-invasively. In the following section our results from the film formation during the growth of the fullerene C_{60} is compared to the post-growth film morphology. Figure 1(a) shows the anti-Bragg intensity during the growth for C_{60} on mica for a substrate temperature of 60 °C and a deposition rate of 1 Å/min. The anti-Bragg intensity oscillates with a period of two monolayers (ML) as consecutive C_{60} layers alternately interfere destructively and constructively. The strong growth oscillations indicate layer-by-layer growth in agreement with previous studies [9, 11], while the observed damping of the growth oscillations after the first three layers shows the onset of slight roughening (see also the time-dependent film roughness in Fig. 1(b)).

For a quantitative analysis of the time-dependent X-ray data the anti-Bragg intensity I_{ab} can be calculated in kinematic approximation by

$$I_{ab}(t) = |A_{sub}\, e^{i\varphi_{sub}} - F_{mol}\sum_{n=1}\theta_n(t)\, e^{i\pi n}|^2, \qquad (1)$$

with $\theta_n(t)$ being the layer coverages for the n-th-layer at time t. The substrate amplitude A_{sub}, the substrate phase φ_{sub} and the molecular form factor F_{mol} can be directly determined from the anti-Bragg intensity [22]. To model the coverages $\theta_n(t)$ as a function of time we employ a mean-field analytical model which was introduced by Trofimov et al. [23] and Woll et al. [24]. This model has already been shown to yield reliable results in organic growth studies when compared to other techniques such as AFM, and quantitative agreement between layer coverages as well as roughness values has been established in Refs. [24–26].

From the evolution of anti-Bragg intensity, we can extract the adsorption probability, which is found to decrease during the growth of the first four layers. Quantitatively,
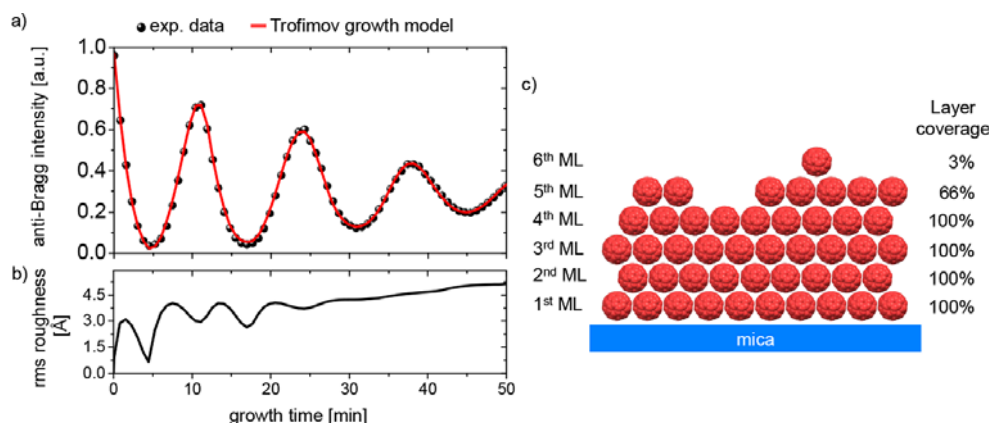
Figure 1 (a) Anti-Bragg intensity as a function of growth time for growth of C_{60} on mica for a substrate temperature of 60 °C, (b) rms film roughness deduced from the Trofimov growth model and (c) schematic view of the layer coverage after 28 min growth.
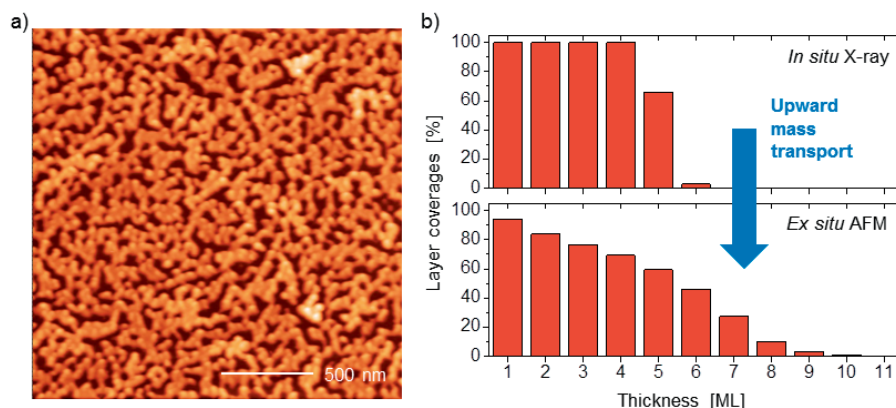
Figure 2 (a) Atomic-force microscopy (AFM) image of a 4.5 ML C_{60} thin film collected 12 h after the deposition at 60 °C. The morphology has an rms roughness of 24 Å. (b) Histograms of the layer coverages of the *in situ* X-ray experiments compared with the layer coverages derived from the *ex situ* AFM image. Note that the amount of molecules agrees in both the AFM and the X-ray measurement but the layer distribution is changed.

we find for the temperature of 60 °C that the adsorption probability decreases by 4% in the 2nd ML, 5% in the 3rd ML and 25% from the 4th layer onwards. This decrease can be attributed to the different mica–C_{60} and C_{60}–C_{60} interactions. Furthermore, it is influenced by a change of the aggregation behavior and of consecutive layers, as the island density and therefore the time until a C_{60} molecule is bound to an island is different in each layer [9].

Also, the layer coverages can be used to calculate the root-mean-square (rms) roughness at each point in time during growth [27]. In Fig. 1(b), the film roughness in nm as a function of time is shown. The first three monolayers grow in a nearly perfect layer-by-layer fashion, indicated by the distinct oscillating behavior of the film roughness between smooth closed layers and rough partially filled layers. The film roughness increases and the roughness does not oscillate, once the perfect layer-by-layer growth gives way to a more 3d growth mode where more than one ML grows simultaneously. Despite the onset of roughening, the absolute film roughness of approx. 4.5 Å (approx. 1/2 ML) for the 8th ML shows that the molecular thin film nevertheless is extraordinarily smooth. The model predicts that the first monolayer is filled 99% before the first 1% of the second monolayer is nucleated. The layer coverage for a later growth stage is illustrated in Fig. 1(c). At a nominal thickness of 4.5 ML (28 min), the 5th and the 6th monolayers grow simultaneously.

In addition to the real-time observation of smooth growth behavior, we studied the film *ex situ* with AFM. Figure 2(a) shows an AFM image of 4.5 ML of C_{60} on mica, which previously was grown at 60 °C with 1 Å/min and then kept at room temperature for 12 h. Interestingly, instead of the smooth molecular film seen during growth, in the AFM image a rough film full of islands and grooves in between is observed. The rms-roughness of the AFM topography is 24 Å and, hence, is six times larger than the rms-roughness identified with the anti-Bragg growth oscil-

lations. Figure 2(b) depicts histograms of the layer coverages of the *ex situ* AFM image compared with the layer coverages derived from the *in situ* X-ray experiments. The histogram of the AFM image shows the formation of islands with up to 10 ML thickness. Note, that the overall amount of material is identical for the result from the X-ray and AFM measurements, but clearly the out-of-plane morphology has changed. The clear discrepancy between the *in situ* real-time growth experiment and the *ex situ* AFM image shows that upward mass transport due to post-growth dewetting has occurred, which agrees with previous findings for thinner films [17]. As the surface energy of mica is lowered by water [28], the dewetting visible in the AFM image may be induced by atmospheric humidity and the displacement of C_{60} through water at the mica surface. The dewetting of C_{60} on a mica surface therefore has to be studied *in situ*.

To not only observe but also quantify the time- and temperature-dependent characteristics of post-growth dewetting *in situ*, we monitored the anti-Bragg intensity during and after the growth of the first monolayer. Figure 3(a) shows the anti-Bragg intensity (grey dots) for the temperatures of 40 °C, 60 °C and 80 °C during growth of the first monolayer, as well as during the subsequent post-growth dewetting. The anti-Bragg intensity drops as the first molecules are deposited on the substrate. After the deposition of the first monolayer the molecular flux was stopped. For all temperatures an increase of the anti-Bragg intensity after the end of deposition is observed. This is due to post-growth dewetting, which causes a mass transport of molecules from the first monolayer into the second layer and, subsequently, the scattered anti-Bragg intensity increases. For the quantification of dewetting we use a simple model. Only the layer coverages θ_1 and θ_2 are considered and we assume a constant amount of molecules after the growth $(\theta_0 = \theta_1(0) + \theta_2(0))$ neglecting desorption processes. The lack of desorption is confirmed through
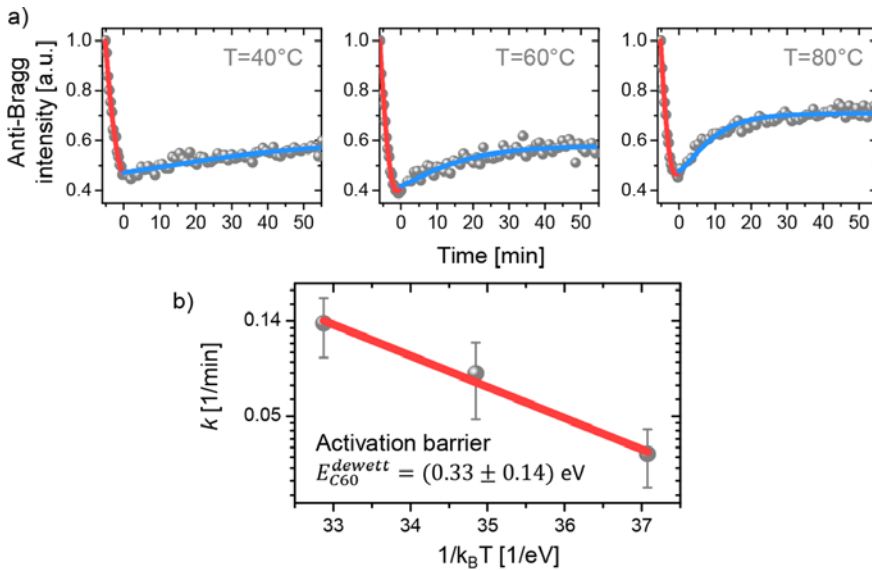
Figure 3 (a) Anti-Bragg intensity for the growth of the first monolayer as well as the post-growth dewetting for 40 °C, 60 °C and 80 °C. (b) Arrhenius type temperature behavior of the dewetting rate yields an effective activation barrier for C_{60} upward transport of (0.33 ± 0.14) eV.

X-ray and AFM measurements in Fig. 2 showing identical amounts of molecules before and after dewetting. Using an intentionally simple rate equation with a single time constant for the second layer coverage during dewetting, the time-dependent exponential function $\theta_2(t) = \theta_2(\infty) - (\theta_2(\infty) - \theta_2(0))\, e^{-t \cdot k}$ is deduced to describe the coverage increase of the second layer. The saturation coverage after the dewetting is described through $\theta_2(\infty)$ and $\theta_2(t_0 = 0)$ is the value for the initial coverage before dewetting. The rate constant of the dewetting process is denoted by k. Importantly, the scattered anti-Bragg intensity of the post-growth dewetting phase can then be fitted by

$$I_{ab}^{dewetting}(t) = |A_{sub}\, e^{i\varphi_{sub}} - F_{mol}[\theta_1(t) - \theta_2(t)]|^2 , \qquad (2)$$

where A_{sub}, φ_{sub} and F_{mol} correspond to the same quantities during growth as in Eq. (1). The overall amount of molecules θ_0 and the initial coverage of the second monolayer before dewetting, $\theta_2(0)$, can be easily taken from the fitting the anti-Bragg oscillation of the first-layer growth. Thus, the rate constant k and the second layer saturation coverage $\theta_2(\infty)$ remain as fitting parameters for dewetting.

In Fig. 3(a), fits of the growth (red, Eq. (1)) and the dewetting (blue, Eq. (2)) for 40 °C, 60 °C and 80 °C are shown. An excellent agreement between experimental data and fits is possible with our model. The resulting rate constant k, the corresponding time $\tau = 1/k$ and the average upward mass transport are summarized in Table 1 for the three temperatures. The average upward mass transport rate is calculated from the mass transport $\Delta\theta_2 = \theta_2(t = \tau) - \theta_2(t = 0)$ in the time interval τ. A temperature increase of 40 K results in an almost five times larger upward mass transport from the first into the second layer.

The thermally-activated mass transport from the first into the second monolayer follows an Arrhenius type be-

Table 1 Upward mass transport rate, rate constant and the corresponding time for the post-growth dewetting process as function of temperature.

temperature T (°C)	upward mass transport $\Delta\theta_2/\Delta t$ (ML/min)	rate constant k (1/min)	time τ (min)
40	0.0044	0.03	33
60	0.0087	0.08	13
80	0.0205	0.13	8

havior (see Fig. 3(b)) [29]

$$k = A \exp\left(-\frac{E_{C60}^{dewetting}}{k_B T}\right). \qquad (3)$$

From fitting the rate k as a function of the inverse temperature, we estimate an effective activation barrier $E_{C60}^{dewetting}$ for C_{60}-dewetting to (0.33 ± 0.14) eV and an effective attempt frequency A of 100 Hz.

4 Discussion For an understanding of the effective activation barrier and the attempt frequency, several contributions to the post-growth dewetting have to be considered. The rate constant k for upward transport is influenced by the C_{60}-mica interaction, the geometry of islands, and the balance of upward and downward diffusion of molecules across the step edge at an island boundary. Morphologies with a large ratio of edge to surface, e.g. dendritically shaped islands, feature more possibilities for molecules to ascend and therefore a higher rate should be expected. Note also that island morphology and their surface area changes during the dewetting process. Therefore, the observed results describe the macroscopic evolution of surface morphology. Correspondingly, k describes the dewetting process as an activated process in a coarse-grained configuration space. The good fit of k as an Ar-

rhenius rate indicates that the layer-by-layer configuration corresponds to a local minimum in configuration space, while the dewetted island configuration forms a deeper energetic minimum. Note that this good Arrhenius fit is not self-evident, as it is not obvious that the potential landscape features characterizing dewetting can be projected onto a single reaction coordinate without loss of relevant information [30, 31]. The net upward mass transport given through k is the difference between the descending and the ascending molecular current. The effective attempt frequency can be considered as a net transport rate for high temperatures, while the effective energy barrier is an activation barrier that reflects the temperature-dependency of dewetting (see Eq. (3)). This temperature-dependency contains the temperature-dependent macroscopic differences in the surface morphology as well as the temperature-dependence of microscopic diffusion- and step-edge crossing processes during dewetting.

The occurrence of the energetically favored island configuration after the growth can have different reasons. First, it could be attributed to C_{60} lattice strain in the very first layers due to lattice mismatch between mica and the epitaxial C_{60} layer. After the growth is stopped molecules tend to release the strain by forming energetically favorable multilayer islands with lower strain in upper layers. This could be important for our epitaxial C_{60} films on mica, as a lateral lattice mismatch of 3.5% has been observed between C_{60} and mica lattice planes [32]. Second, the change of morphology could be further influenced by a change of surface energy balance after growth is stopped as proposed by Burke et al. [17] for C_{60} on alkali halides surfaces. The continuous molecular exposure causes the formation of a 2D gas on the surface. Therefore, the absence of this 2D vapor pressure through the interruption of growth can result in the change of the mica surface energy. Accordingly, the changed balance of surface energies causes a transition from layer to island formation. Our finding that smooth multi-layer films of C_{60} are built up in a layer-by-layer fashion during growth and that the thin film morphology changes completely once the growth is stopped could be an indication for such a 2D vapor pressure induced growth behavior. The post-growth dewetting phenomena reflect the non-equilibrium character of the growth process [33]. The continuous molecular exposure impinging the surface (even at low deposition rate) makes growth kinetically limited and enables the formation of thermodynamically unstable transient structures [33].

For a more detailed understanding of the thermodynamic stability of C_{60}-films on mica, additional insight into the volume and surface phase diagrams, including the (pre-) wetting line is needed. Theoretically, wetting phase diagrams similar to the present case of C_{60} can be studied using the mean-field Cahn-Landau theory [34] or the more microscopic classical density-functional-theory [35, 36]. Further, we refer to recent research on non-equilibrium wetting/dewetting via the Edwards-Wilkinson and the Kardar–Parisi–Zhang equation [37, 38]. All approaches require a precise knowledge of the thermodynamic potential as function of a suitable reaction coordinate. The resulting free energy landscape could eventually contribute to an understanding of the thermally-activated mass transport.

5 Conclusion We have studied the temperature-dependent kinetics of the growth and post-growth dewetting process of the fullerene C_{60} on mica in ultra-thin films by real-time X-ray scattering. Smooth multilayer films form in a layer-by-layer fashion during growth as observed with *in situ* experiments. We observe a thermally-activated dewetting behavior for the first monolayer and we find that a temperature increase of 40 K results in a five-times faster upward mass transport. An effective activation barrier for upward interlayer transport of $((0.33 \pm 0.14)$ eV describing the temperature-dependent macroscopic changes of the surface morphology is estimated for the first time. Our findings are a first example for detailed quantification of thermal stability of molecular thin film and, therefore, contribute to the understanding of functional molecular materials and their long-term (morphological) stability.

References

[1] A. Opitz, J. Wagner, W. Brütting, I. Salzmann, N. Koch, J. Manara, J. Pflaum, A. Hinderhofer, and F. Schreiber, IEEE J. Sel. Top. Quantum Electron. **16**, 1707 (2010).

[2] M. Gruber, M. Rawolle, J. Wagner, D. Magerl, U. Hörmann, J. Perlich, S. V. Roth, A. Opitz, F. Schreiber, P. Müller-Buschbaum, and W. Brütting, Adv. Energy Mater. **3**, 1075 (2013).

[3] B. Verreet, P. Heremans, A. Stesmans, and B. P. Rand, Adv. Mater. **25**, 5504 (2013).

[4] W. Krakow, N. M. Rivera, R. A. Roy, R. S. Ruoff, and J. J. Cuomo, J. Mater. Res. **7**, 784 (1992).

[5] J. Yang, D. Yan, and T. S. Jones, Chem. Rev. **115**, 5570 (2015).

[6] D. Käfer, L. Ruppel, and G. Witte, Phys. Rev. B **75**, 085309 (2007).

[7] G. Hlawacek, P. Puschnig, P. Frank, A. Winkler, C. Ambrosch-Draxl, and C. Teichert, Science **321**, 108 (2008).

[8] S. Yim and T. S. Jones, Appl. Phys. Lett. **94**, 021911 (2009).

[9] S. Bommel, N. Kleppmann, C. Weber, H. Spranger, P. Schäfer, J. Novak, S. V. Roth, F. Schreiber, S. H. L. Klapp, and S. Kowarik, Nature Commun. **5**, 5388 (2014).

[10] L. Pithan, C. Cocchi, H. Zschiesche, C. Weber, A. Zykov, S. Bommel, S. J. Leake, P. Schäfer, C. Draxl, and S. Kowarik, Cryst. Growth Des. **15**, 1319 (2015).

[11] S. Yaginuma, K. Itaka, M. Haemori, M. Katayama, K. Ueno, T. Ohnishi, M. Lippmaa, Y. Matsumoto, and H. Koinuma, Appl. Phys. Express **1**, 015005 (2008).

[12] J. Yang, S. Yim, and T. S. Jones, Sci. Rep. **5**, 9441 (2015).

[13] A. Turak, RSC Adv. **3**, 6188 (2013).

[14] S. A. Burke, J. M. Topple, and P. Grütter, J. Phys.: Condens. Matter **21**, 423101 (2009).

[15] S. Kowarik, A. Gerlach, S. Sellner, L. Cavalcanti, and F. Schreiber, Adv. Eng. Mater. **11**, 291 (2009).

[16] A. Amassian, V. A. Pozdin, T. V. Desai, S. Hong, A. R. Woll, J. D. Ferguson, J. D. Brock, G. G. Malliaras, and J. R. Engstrom, J. Mater. Chem. **19**, 5580 (2009).

[17] S. Burke, J. Mativetsky, S. Fostner, and P. Grütter, Phys. Rev. B **76**, 035419 (2007).

[18] M. Körner, F. Loske, M. Einax, A. Kühnle, M. Reichling, and P. Maass, Phys. Rev. Lett. **107**, 016101 (2011).

[19] M. Dresselhaus, G. Dresselhaus, and P. Eklund, Science of Fullerenes and Carbon Nanotubes (Academic Press, San Diego, USA, 1996).

[20] F. Ostendorf, C. Schmitz, S. Hirth, A. Kühnle, J. J. Kolodziej, and M. Reichling, Nanotechnology **19**, 305705 (2008).

[21] A. Buffet, A. Rothkirch, R. Döhrmann, V. Körstgens, M. M. Abul Kashem, J. Perlich, G. Herzog, M. Schwartzkopf, R. Gehrke, P. Müller-Buschbaum, and S. V. Roth, J. Synchrotron Radiat. **19**, 647 (2012).

[22] S. Kowarik, A. Gerlach, M. W. A. Skoda, S. Sellner, and F. Schreiber, Eur. Phys. J. Spec. Top. **167**, 11 (2009).

[23] V. I. Trofimov and V. G. Mokerov, Thin Solid Films **428**, 66 (2003).

[24] A. R. Woll, T. V. Desai, and J. R. Engstrom, Phys. Rev. B **84**, 075479 (2011).

[25] C. Weber, C. Frank, S. Bommel, T. Rukat, W. Leitenberger, P. Schäfer, F. Schreiber, and S. Kowarik, J. Chem. Phys. **136**, 204709 (2012).

[26] C. Frank, J. Novák, R. Banerjee, A. Gerlach, F. Schreiber, A. Vorobiev, and S. Kowarik, Phys. Rev. B **90**, 045410 (2014).

[27] S. Kowarik, A. Gerlach, and F. Schreiber, J. Phys.: Condens. Matter **20**, 184005 (2008).

[28] H. K. Christenson, J. Phys. Chem. **97**, 12034 (1993).

[29] S. Arrhenius, Z. Phys. Chem. **4**, 226 (1889).

[30] T. Heinemann, K. Palczynski, J. Dzubiella, and S. H. L. Klapp, J. Chem. Phys. **141**, 214110 (2014).

[31] D. Bonn, J. Eggers, J. Indekeu, J. Meunier, and E. Rolley, Rev. Mod. Phys. **81**, 739 (2009).

[32] J. E. Fischer, E. Werwa, and P. A. Heiney, Appl. Phys. A **56**, 193 (1993).

[33] H. Brune, in: Surface and Interface Science, edited by K. Wandelt, Solid-Solid Interfaces and Thin Films, Vol. 4 (Wiley-VCH Verlag, Weinheim, 2013).

[34] D. Bonn and D. Ross, Rep. Prog. Phys. **1085**, 1085 (2001).

[35] S. Dietrich, in: Wetting Phenomena, edited by C. Domb and J. L. Lebowitz, Phase Transitions and Critical Phenomen, Vol. 12 (Academic Press, London, 1988).

[36] D. E. Sullivan, and M. M. Telo da Gama, Fluid Interfacial Phenomena, in: Wetting Transitions and Multilayer Adsorption at Fluid Interfaces, edited by C. A. Croxton (Wiley, New York, 1986), chap. 2.

[37] F. de los Santos, M. M. Telo da Gama, and M. A. Muñoz, Phys. Rev. E **67**, 021607 (2003).

[38] H. Hinrichsen, R. Livi, D. Mukamel, and A. Politi, Phys. Rev. E **68**, 041606 (2003).